Materials Horizons

ROYAL SOCIETY OF CHEMISTRY

COMMUNICATION

View Article Online
View Journal

Cite this: DOI: 10.1039/d6mh00036c

Received 8th January 2026,
Accepted 30th March 2026

DOI: 10.1039/d6mh00036c

rsc.li/materials-horizons

Friction-assisted electrochemical oxidation of iridium surfaces for enhanced catalysis

Chenxu Liu,†*[ab] Johannes L. Hörmann, †[cde] Haoran Pan,†[f] Hantao Xu,[g] Lianhuan Han, [h] Jun Cheng, [g] Xingxing Chen,*[f] Hongbo Zeng, *[b] Yonggang Meng*[a] and Yu Tian*[a]

Iridium oxide (IrO_x) has emerged as a prominent catalyst for the acidic oxygen evolution reactions (OER). However, its direct preparation on the surface of Ir is rare, severely restricting its applications in catalysis and sensing technologies. In this work, we report an innovative method to locally generate amorphous IrO_x layers on Ir surfaces through the synergistic action of friction and anodic potentials. This approach enables the rapid preparation of sub-micrometer-thick IrO_x layers within 200 s. The microscopic topography of the Ir substrate has a significant impact on local reactant surface excess. Additionally, friction lowers the surface potential required for the oxidation of Ir and also introduces defects that enhance the electrocatalytic activity of the oxide. The resulting IrO_x characterized by unique nanostructures demonstrates significant OER activity in acidic environments, significantly surpassing that of metallic Ir. These findings highlight the great potential of friction-assisted anodization for advancing micro-reactors and micro-sensor arrays.

New concepts

Direct formation of iridium oxide (IrO_x) on metallic iridium is rarely reported, despite its considerable potential in catalysis and pH sensing applications. Here, we present a novel strategy for the localized generation of IrO_x layers on rough Ir surfaces through the synergistic action of friction and anodic polarization. The resulting IrO_x exhibits nanostructured features with characteristic diameters of 1–5 nm, and its thickness can reach sub-micrometer scales within 200 seconds. We show that the microscopic geometry of the Ir substrate critically governs the local surface excess of reactive species, thereby influencing oxide growth. Moreover, friction not only reduces the effective surface potential required for Ir oxidation but also induces structural defects that markedly enhance the electrocatalytic activity of the resulting IrO_x. Owing to its distinctive nanostructure and electrochemical activity, the friction-induced IrO_x displays substantially higher reactivity than metallic Ir, highlighting its promise for applications in sensor arrays and micro-reactors. Beyond demonstrating an unconventional oxidation pathway for chemically inert Ir under coupled mechanical and electrical stimuli, this work provides a generalizable approach for engineering oxide catalysts with tailored structures and functionalities.

Introduction

Water electrolysis driven by renewable power sources is one of the cornerstones in energy conversion and storage technologies.[1–3] The anodic reaction, known as the oxygen evolution reaction (OER), is crucial because it supplies the protons and electrons required for these processes.[4] Among the various materials capable of catalysing the OER, iridium oxide (IrO_x) stands out as the only practical industrial electrocatalyst that combines high catalytic activity for oxygen evolution with considerable stability, even under harsh acidic conditions.[2,5–8]

Due to the ultralow-earth abundance of Ir, it should be used at low loading to advance the scalability of water electrolysis.[9] To improve the catalytic efficiency of Ir-based oxides, extensive efforts have been devoted to strategies, such as surface restructuring[10], amorphization,[1,11] and heteroatom doping.[5,12,13]

[a] State Key Laboratory of Tribology in Advanced Equipment, Tsinghua University, Beijing 100084, China. E-mail: liuchenxu19910407@163.com, mengyg@tsinghua.edu.cn, tianyu@mail.tsinghua.edu.cn
[b] Department of Chemical and Materials Engineering, University of Alberta, Edmonton, Alberta T6G 1H9, Canada. E-mail: hongbo.zeng@ualberta.ca
[c] Department of Microsystems Engineering, University of Freiburg, Georges-Köhler-Allee 103, 79110 Freiburg, Germany
[d] Cluster of Excellence livMatS, Freiburg Center for Interactive Materials and Bioinspired Technologies, University of Freiburg, Georges-Köhler-Allee 105, 79110 Freiburg, Germany
[e] Department of Complex Systems Science, Graduate School of Informatics, Nagoya University, Furo-cho, Chikusa-ku, Nagoya 464-8601, Japan
[f] Research Institute of Clean Energy and Fuel Chemistry, School of Chemical Engineering, University of Science and Technology Liaoning, Anshan 114051, China. E-mail: xingchenstar@ustl.edu.cn
[g] Department of Chemistry, College of Chemistry and Chemical Engineering, Xiamen University, Xiamen 361005, China
[h] Department of Mechanical and Electrical Engineering, Pen-Tung Sah Institute of Micro-Nano Science and Technology, Xiamen University, Xiamen 361005, China
† These authors contributed equally to this work.

Among these, amorphous IrO_x has attracted particular attention because its disordered local structure, abundant oxygen vacancies, and unsaturated coordination environments can promote the adsorption and transformation of OER intermediates more effectively than crystalline IrO_2.[11,13–15] Recent advances have demonstrated that amorphous IrO_2 and related composite catalysts can achieve high OER activity, often through multimetal doping or complex synthetic protocols that tailor the local structure and electronic properties of active sites.[16–19] Despite their effectiveness, these strategies typically rely on elaborate compositional design. Therefore, it remains of considerable interest to explore whether comparable catalytic performance can be achieved through a simpler route based primarily on structural modulation, rather than chemical complexity. This motivates the development of alternative methods for generating highly active Ir-based oxide catalysts with unique disordered structures.

Elastic–plastic deformation caused by friction generally increases defects or grain boundaries on solid surfaces or sub-surfaces. Building upon this concept, surface mechanical attrition treatment has been developed, which induces grain refinement to the nanometer scale within the surface layer of bulk metals.[20,21] This enables the fabrication of various novel gradient metals with unique mechanical properties.[22,23] However, directly introducing defects into IrO_x through friction is unsuitable due to the brittleness of the ceramic, which risks fracture.

By combining anodic oxidation with friction processing, we developed a novel approach to locally prepare IrO_x layers with specialized nanostructures directly on Ir surfaces. Typically, oxide films exceeding a few nanometers are difficult to form on Ir surfaces within conventional electrochemical systems. However, the thickness of the IrO_x layer, achieved under anodic potentials during friction with a ceramic ball, could attain a sub-micrometer scale within only 200 s. Simulations explored the effects of roughness on electric field distribution and the concentration of key reactants, while experiments assessed the impact of friction on electrode kinetics. Friction not only lowered the surface potential required for Ir electrochemical oxidation but also introduced defects that enhanced the catalytic activity of the product. High-resolution transmission electron microscopy (HRTEM) revealed that the IrO_x layer consisted of amorphous oxide encapsulating Ir nanocrystals, forming a unique structure, which exhibited remarkable electrocatalytic activity and stability in harsh acidic conditions.

Compared with traditional methods for preparing IrO_x, such as electrodeposition,[1,24] pulsed laser deposition,[25,26] sputtering[27], spray pyrolysis[28], thermal oxidation[29], pyrolysis[30] and molten-salt method[31], this method provides a localized route for IrO_x generation directly on Ir surfaces. More importantly, it highlights friction-induced amorphization as a simple yet effective alternative to conventional multimetal doping and sophisticated synthetic protocols for activating Ir-based catalysts. This strategy not only enhanced OER performance but also opens new opportunities for extending IrO_x applications to neural electrodes,[32,33] micro-reactors, and sensors[34].

Results and discussion

Characterization of the IrO_x layer

IrO_x was fabricated on selected Ir surfaces using a tribo-electrochemical method, performed with a tribometer equipped with an electrochemical workstation. A schematic illustration of the experimental setup for this method is provided in Fig. S1. Ir is an inert metal and is difficult to oxidize through traditional electrochemical processes. However, it has been observed that under friction forces, the electrochemical potential window changes,[35,36] making surface oxidation of Ir possible. Interestingly, the roughness of the initial surface plays a significant part in influencing the oxidation of Ir.

To maintain consistency in experimental parameters, we selected samples with surfaces that were half smooth (R_a = 9 nm) and half rough (R_a = 43 nm). During the friction test, the upper friction pair (ZrO_2 ball) was exposed to the smooth and rough regions on the surface of the lower friction pair (Ir plate). The applied load was set at 4 N, the sliding velocity at 24 mm s^{-1}, and the testing time was 200 s. The surface potential of the lower friction pair was maintained at +0.6 V throughout the test. After the friction test, surface observations inside and outside the wear track are presented in Fig. 1a. A significant amount of black material was generated on the rough region of the Ir surface, whereas almost no material formed on the smooth side.

Subsequently, we analysed the surface morphology and composition of the wear tracks on the rough and smooth surfaces using scanning electron microscopy (SEM) combined with energy-dispersive X-ray spectroscopy (EDS), as shown in Fig. 1b–e. For the rough surface, a substantial presence of oxygen was detected within the wear track, while the smooth surface exhibited negligible amounts. This indicated that the black substances observed in Fig. 1a were oxides, predominantly forming on rough Ir surfaces. The width of the wear track was $\sim$150 μm. The composition and distribution inside and outside the wear track were characterized using Raman spectroscopy, as shown in Fig. 1f and g. The blue curve in Fig. 1f reveals a prominent characteristic peak at 450 cm^{-1}, which is indicative of Ir oxide present within the wear track.[6,37,38] In contrast, the red curve, which lacks this characteristic peak, suggests that the regions outside the wear track had not undergone oxidation. Fig. 1g demonstrates that the distribution of the black material region on the rough Ir surface aligns with the Raman spectral characteristic peaks. The width of the feature region was $\sim$150 μm, consistent with the EDS result shown in Fig. 1c. Quantitative image analysis showed that the IrO_x layer covered 26.1 $\pm$ 4.1% of the wear-track region, indicating partial, but clearly localized, oxidation within the friction-affected area.

Furthermore, we focused on analysing the depth profile of the oxide within the wear track. This was initially investigated using sputtering X-ray photoelectron spectroscopy (XPS). The Ir 4f peaks at 60.79 eV and 63.82 eV were assigned to Ir, as shown in Fig. 1h. Additionally, peaks at 61.66 eV and 64.68 eV corresponded to IrO_2.[39] With increased sputtering depth,

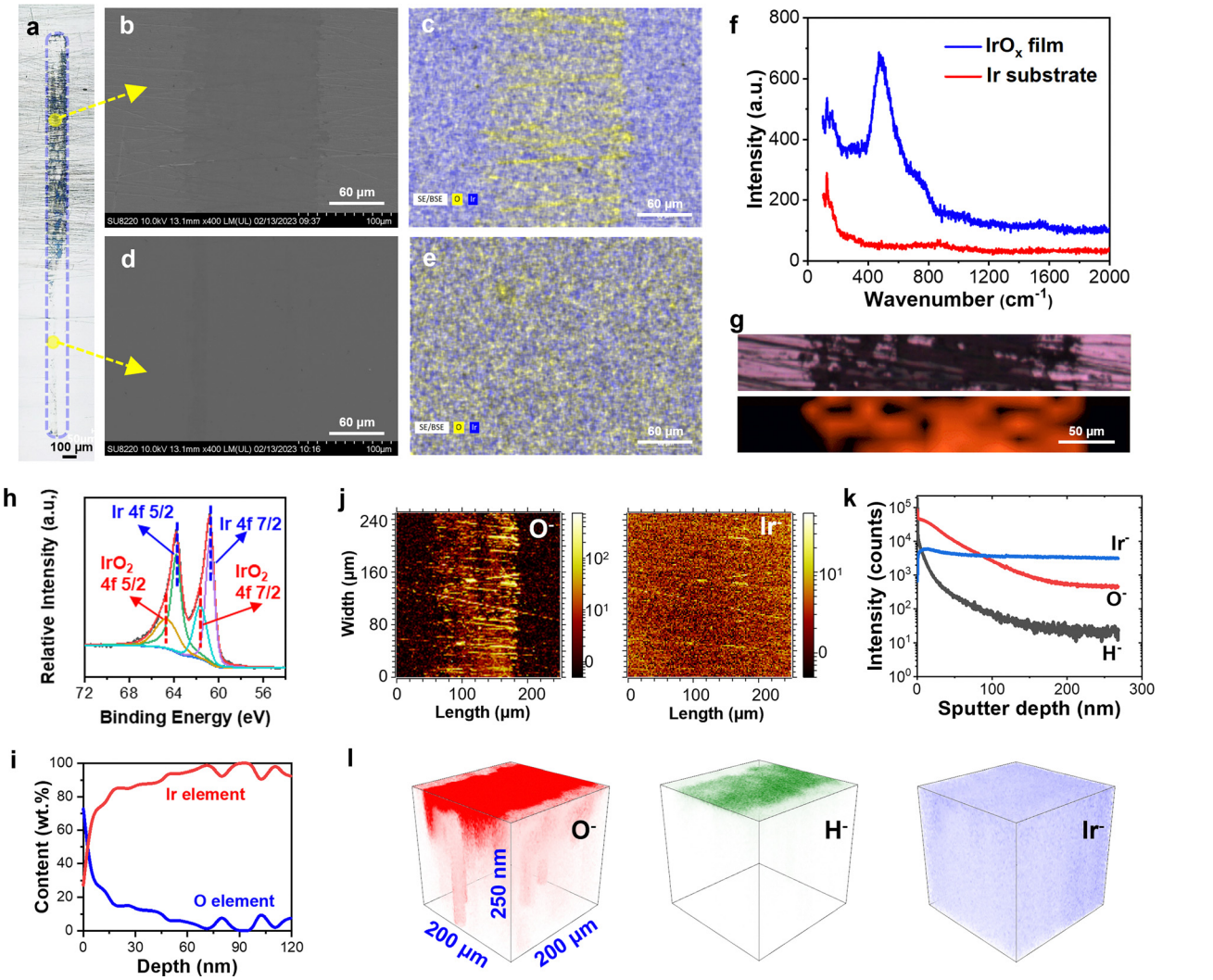

Fig. 1 Morphology and composition characterization of the wear track after tribo-electrochemical reactions. (a) Macroscopic image of a wear track on a surface with smooth and rough regions. (b) and (c) show the microstructure and elemental distribution of the wear track on the rough surface, while (d) and (e) present the corresponding data for the smooth surface. (f) Raman spectrum recorded inside and outside the wear track, highlighting the presence of an IrO_x tribofilm within the wear track and Ir substrate outside of it. (g) Spatial distribution of Raman characteristic peaks inside and outside the wear track. (h) XPS of the Ir 4f of the original wear surface on the lower friction pair. (i) XPS profile of O and Ir elements during monatomic Ar^+ etching of the tribofilm. (j) 2D ToF-SIMS displaying the distributions of chemical fragments within wear tracks. (k) ToF-SIMS intensity spectra revealing the chemical composition of the IrO_x layer as a function of depth. (l) 3D ToF-SIMS characterization of the IrO_x layer.

the oxygen content gradually decreased, becoming nearly negligible below ~60 nm (Fig. 1i and Fig. S2). The composition of oxides was further analysed using time of flight secondary ion mass spectrometry (ToF-SIMS). As illustrated in Fig. 1j, it presented across the entire surface, while oxygen was primarily concentrated within the wear track. To more accurately calculate the sputtering rate, we measured the depth of the tested area after 1200 s of the ToF-SIMS test.

Based on the data shown in Fig. S3, we determined the sputtering rate to be 0.21 nm s^{-1} (1200 s, 250 nm). According to Fig. 1k, as the sputtering depth increased from 0 to 250 nm, the Ir content remained relatively constant, while the concentrations of O and H gradually declined, stabilizing at ~100 nm. This trend was consistent with XPS findings (Fig. S2). Fig. 1l provides a more visual representation of the spatial distribution of O, H, and Ir. Notably, the H concentration on the wear mark surface was relatively high, likely due to the presence of OH^- groups and/or H_2O adsorption. The O content was more prominent in deeper regions, particularly within the first 70 nm, further confirming the previous analysis. Based on these results, a 70-nm-thick oxide film of width 150 μm formed on the rough Ir surface but not on the smooth surface. Considering that the wear track was typically ~4 mm in length and ~150 μm in width, together with an IrO_x surface coverage of 26.1% and an average thickness of ~70 nm, the total volume of the generated IrO_x was estimated to be $\sim 1.1 \times 10^{-5}$ mm^3.

Additionally, we explored the effects of velocity, normal load, sliding time, and surface potential on the formation of IrO_x tribofilms, as shown in Fig. S4 and S5. These results indicated that oxides formed on the metal surface when the load ranged

from 1 N to 4 N, the surface potential was above +0.6 V, and the velocity lay between 4 mm s^{-1} and 32 mm s^{-1}.

The cross-sectional microstructure and composition of the oxide tribofilm were further analysed using transmission electron microscopy (TEM) and integrated differential phase contrast scanning transmission electron microscopy (iDPC-STEM), following mechanical etching *via* a focused ion beam (FIB). TEM (Fig. 2a) showed the tribo-electrochemical oxidation layer with a thickness ranging from 50 to 100 nm. The morphology and elemental distribution of the tribofilm, measured using EDS, are displayed in Fig. 2b. The analysis revealed that, across the 68-nm thickness of the tribofilm, the Ir content decreased, while the O content increased as the detection moved closer to the rubbing surface. The Cr layer was observed as a protective layer for the FIB process.

A detailed observation at a higher magnification for the selected spot is shown in Fig. 2c. The tribofilm contained nanocrystallites ranging from 1 to 5 nm in diameter, which were confirmed to be non-oxidized Ir clusters located near the centers of the grains. A representative high-resolution transmission electron microscopy (HRTEM) image of ultrafine Ir grains within the tribofilm is provided in Fig. 2d. Element mappings of Ir and O are presented in Fig. 2e and f, respectively. The Ir element was concentrated in the grain interior, while O was predominantly located around Ir grains. Tribological shear-induced plastic deformation, involving high strain

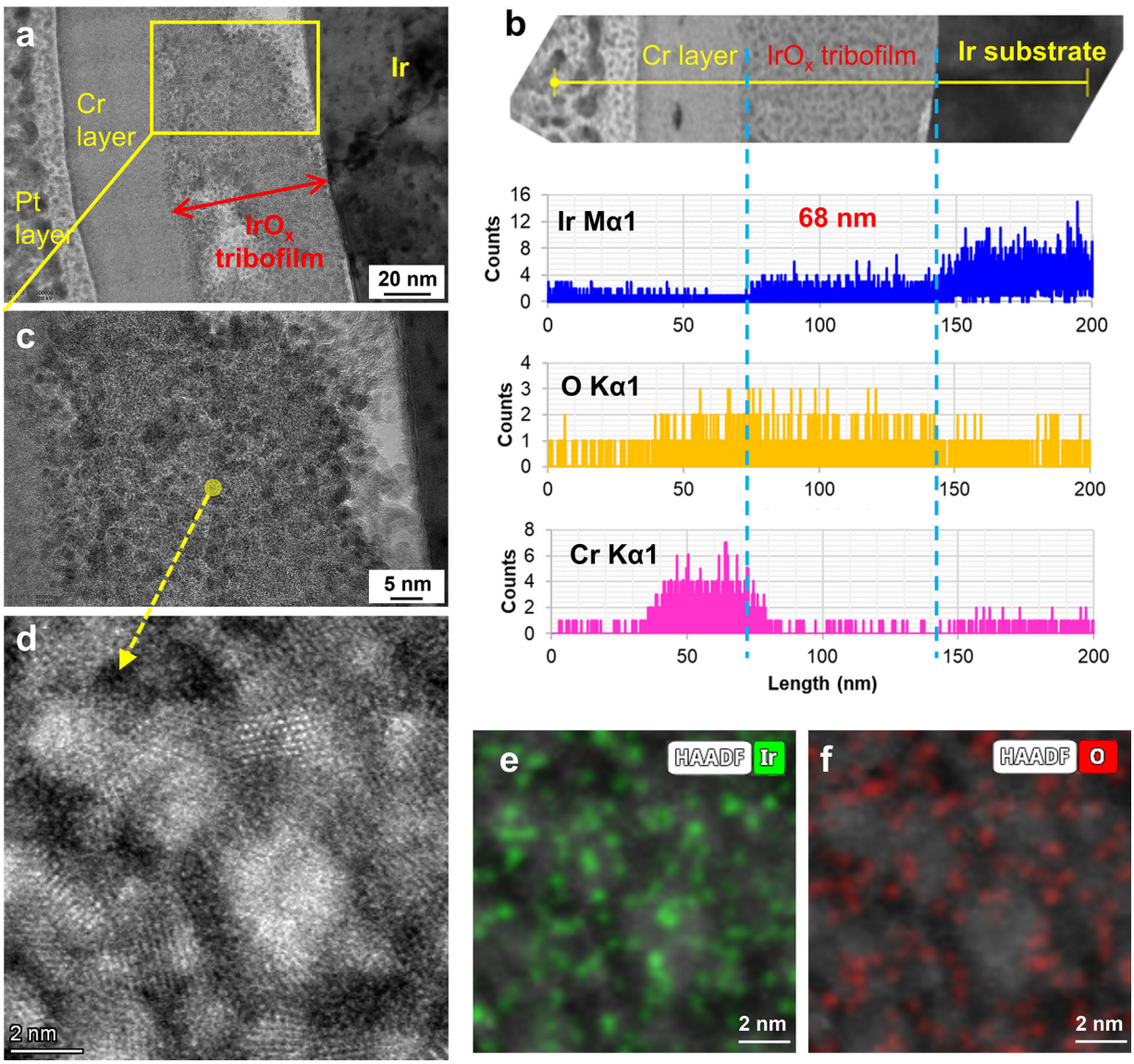

Fig. 2 TEM of the FIB cross-section of the tribofilm on the Ir wear track. (a) Cross-sectional TEM image of the tribofilm. (b) EDS elemental distribution across the tribofilm. (c) Higher-magnification TEM image providing detailed structural information of the tribofilm. (d) HRTEM image showing ultrafine Ir grains in the tribofilm. (e) and (f) represent Ir and O elemental mappings, respectively, with the dark-field image highlighting the Ir grain. The surface potential during the test was +0.6 V (Ag/AgCl reference electrode), and pure water was as used as the electrolyte and lubricant. The test duration was 200 s.

and strain rates, led to nano-twinning-assisted dynamic recrystallization, which resulted in the formation of ultrafine Ir grains within the tribofilm. The oxidation of these ultrafine Ir grains, strongly influenced by O atom diffusion, also impacted grain deformation, ensuring the grain size remained stable within a certain range in the tribofilm.

The friction-induced IrO_x prepared in this work was identified to be an amorphous oxide. Its structural and compositional features were comprehensively characterized by SEM/EDS, XPS, Raman spectroscopy, and FIB-TEM, and confirmed its distinctive morphology and disordered structure (Fig. 1 and 2). The IrO_x layer was generated directly from the Ir substrate during the friction-assisted anodic oxidation process. Hence, it was expected to form strong interfacial bonding with the underlying metal rather than simple physical attachment. This hypothesis was further supported by mechanical and tribological tests. Depth-dependent nanoindentation results (Fig. S6a) showed a smooth transition in hardness and complex modulus from the oxide layer to the substrate, with no delamination or spallation observed during indentation. Moreover, the IrO_x layer remained intact after sliding friction under a normal load of 4 N for 300 s, without detectable peeling or interfacial failure (Fig. S6b). These results demonstrated the robust interfacial adhesion and mechanical integrity of the friction-induced IrO_x layer.

Electrocatalytic performance of the IrO_x layer

Friction enhances the electrochemical reactivity of frictional products during and after the friction process. To validate this hypothesis, we evaluated the electrocatalytic activity of the post-experimental products. To elucidate the electrochemical properties of the IrO_x film produced by tribo-electrochemistry for the OER, linear sweep voltammetry (LSV) was systematically performed by examining various regions of the sample (Fig. 3a). Remarkably, the IrO_x film exhibited exceptional efficiency, requiring an overpotential of only 310 mV to achieve a current density of 10 mA cm^{-2} for the OER. This performance stands out when compared with the reference materials, with IrO_2 requiring an overpotential of 350 mV and metallic Ir demanding 500 mV.

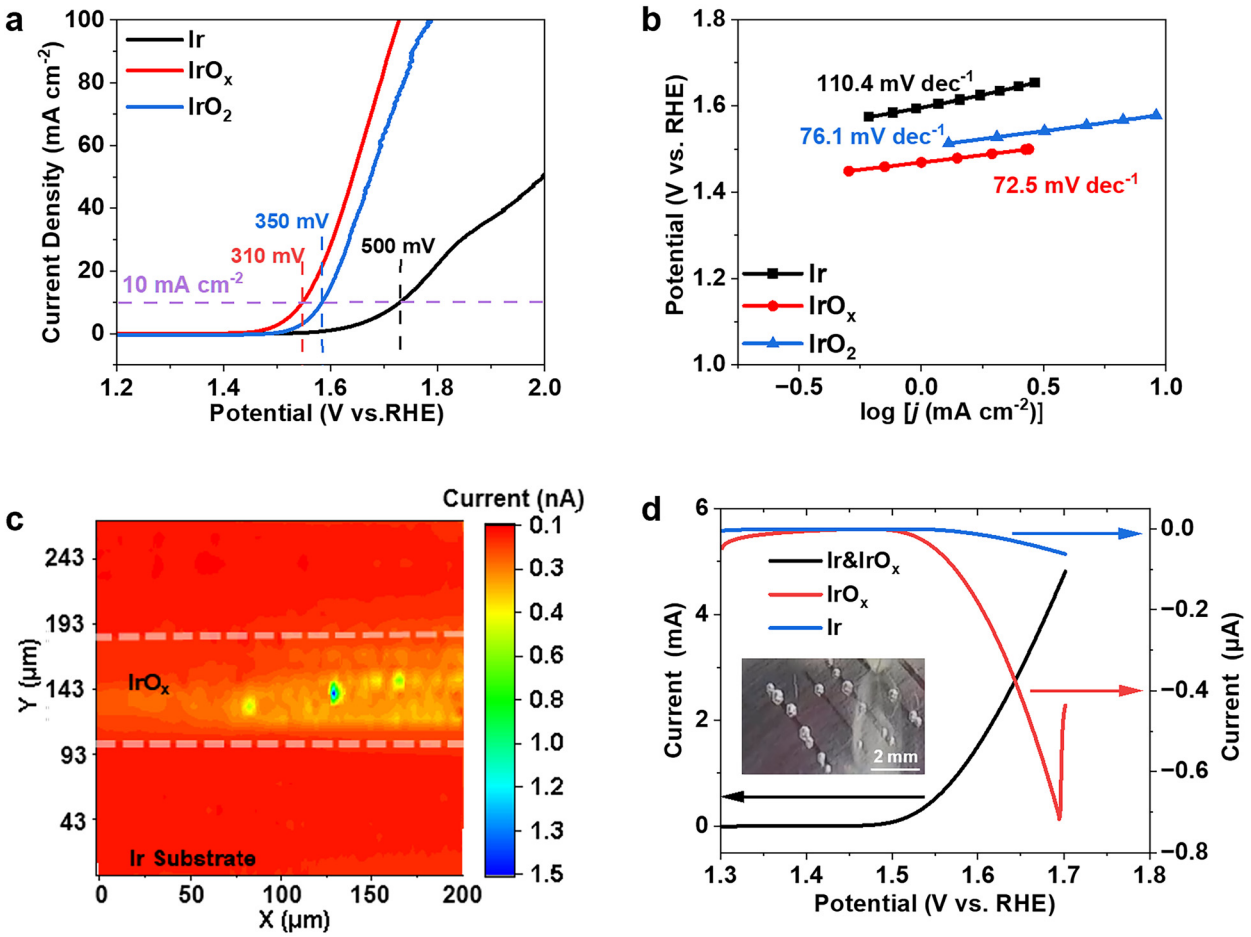

Fig. 3 Electrochemical activity of Ir and IrO_x. (a) LSV curves for the OER recorded in 0.1 M $HClO_4$. (b) Tafel plots comparing the OER performance of Ir–IrO_x, reference IrO_2 and metallic Ir. (c) SECM feedback currents for Ir and IrO_x measured in an electrolyte containing 1 mM $Ru(NH_3)_6Cl_3$ and 0.1 M K_2SO_4, with a Pt UME moving at 20 μm s^{-1} while maintaining a constant 4-μm UME-substrate distance. (d) LSV of Ir–IrO_x recorded between 1.3 V and 1.8 V at a scan rate of 5 mV s^{-1}, with the probe held at 0.11 V in 0.1 M $HClO_4$. The inset in (d) shows a macroscopic image of preferential oxygen evolution on the IrO_x within the wear track, rather than on the surrounding Ir surface.

The Tafel slope is a critical indicator of electrochemical activity and kinetics. The fabricated IrO_x film exhibited a notably lower Tafel slope of 72.5 mV dec^{-1}, apparently lower than the ones of reference IrO_2 (76.1 mV dec^{-1}) and metallic Ir (110.4 mV dec^{-1}) (Fig. 3b), demonstrating its superior electrochemical OER performance.

To investigate in depth the local reactivity differences of IrO_x and reference Ir samples, high-resolution scanning electrochemical microscopy (SECM) in feedback mode was employed to evaluate their heterogeneous electron transfer (HET) reactivity. The OER involves a four-electron proton-coupled reaction, so the HET rate serves as a crucial parameter that characterizes the kinetic behaviour of the reaction. It represents the rate at which electrons are transferred between the catalyst and reactants, thereby influencing the overall catalytic performance.

As shown in Fig. S7, a Pt ultramicroelectrode (UME) of radius 1 μm was used as the tip electrode, while Ir and IrO_x were utilized as substrate materials. To avoid substrate-specific reactions, the $Ru(NH_3)_6Cl_3$ redox couple was selected as the mediator. During SECM, the Pt UME was held at −0.80 V (*vs.* Pt reference electrode), while the substrate remained unbiased. The reduced $Ru(NH_3)_6^{2+}$ species generated at the Pt UME then diffused to the substrate, where they were oxidized back to $Ru(NH_3)_6^{3+}$ by Ir or IrO_x. These oxidized species subsequently returned to the UME for reduction, establishing a positive feedback loop.

The magnitude of the positive feedback current is directly correlated with HET activity. A higher feedback current indicates a faster HET rate. As depicted in Fig. 3c, the feedback current over the Ir region stabilized at ∼0.18 nA, attributable to its relatively smooth surface. In contrast, as the Pt UME approached the IrO_x surface, the current increased significantly, peaking at 0.40 nA—nearly a threefold enhancement. Notably, in certain regions of IrO_x, the feedback current increased by more than sevenfold, reaching as high as 1.44 nA. This enhancement was likely due to the non-uniform growth of IrO_x during the tribo-electrochemical process, which led to localized aggregation and heightened electrochemical activity. These results suggested that the IrO_x within wear track possessed significantly higher OER activity potential.

To further validate the contrast in local activity observed in feedback mode, the OER reactivity of the IrO_x layer under acidic conditions was further investigated using the sample generation-tip collection (SG-TC) mode of SECM. In this mode, IrO_x catalyses the OER at a given potential, generating O_2, which is subsequently collected by the Pt UME through the oxygen reduction reaction (ORR). The resulting cathodic ORR current at the Pt UME therefore serves as a local indicator of O_2 generation, and hence of the OER activity on the substrate. In Fig. 3d, the black line shows the LSV polarization curve of the Ir–IrO_x substrate, while the red and blue lines indicate the ORR currents recorded at the SECM probe (E_{probe} = 0.11 V *vs.* reversible hydrogen electrode, RHE) for IrO_x and background Ir, respectively. A pronounced contrast in tip current was observed between the IrO_x region and background Ir surface. Over IrO_x, a probe current of −48.40 nA was recorded at $E_{substrate}$ = 1.55 V, representing a substantial increase of ∼27.2-fold compared with the −1.78 nA observed over background Ir. These findings confirmed the substantially enhanced local OER activity of friction-induced IrO_x.

At more positive substrate potentials, a decrease in the ORR collection current above IrO_x was observed. This was likely attributable to partial blockage of the probe–substrate gap by detached O_2 bubbles generated from the highly active IrO_x region. Optical imaging further confirmed that oxygen evolution occurred preferentially on IrO_x regions rather than on the surrounding metallic Ir surface (inset in Fig. 3d).

Moreover, the spatial distribution of OER activity across the Ir–IrO_x interface at various potentials was further examined by SECM in SG-TC mode. Fig. S8 presents a schematic of the analysed sample area. To minimize the interference from bubble formation during SECM measurements, sample potentials were carefully selected to be 1.49 V and 1.50 V, close to the OER onset potential for IrO_x. The chromatic variations observed in the resulting spectra indicated local variations in activity, with blue shifts signifying heightened OER activity. Notably, the IrO_x region exhibited markedly superior OER activity compared with Ir, as evidenced by higher current densities in the central area, highlighting the catalytic prowess of IrO_x for the OER. Overall, this SECM approach provided spatially resolved insight into local OER activity that is difficult to obtain from conventional bulk electrochemical measurements.

Cyclic voltammetry at various scan rates in the non-faradaic potential region was performed to estimate the electrochemically active surface area (ECSA) (Fig. S9a–d). Results indicated that the friction-induced amorphous IrO_x thin film exhibited a relatively rougher surface and a larger ECSA than smooth metallic Ir. The substantially higher ECSA of commercial IrO_2 was mainly attributed to its powder-based morphology. When drop-cast onto a glassy carbon electrode, it formed a porous catalyst layer that provided a much larger accessible surface area. After normalization of LSV curves by ECSA, the activity trend remained unchanged from that shown in Fig. 3a, with OER activity following the order IrO_x > IrO_2 > metallic Ir (Fig. S9e). This result confirmed that the superior OER performance of the friction-induced amorphous IrO_x was not solely due to an increased surface area, but also reflected enhanced intrinsic electrocatalytic activity.

Table S1 compares the overpotentials at 10 mA cm^{-2} of recently reported amorphous Ir- or IrO_x-based composites. Results indicated that the friction-induced amorphous IrO_x layer prepared in this work exhibited an overpotential of 310 mV at 10 mA cm^{-2}, which is comparable with those of reported amorphous Ir- or IrO_x-based composites modified with other metallic elements.[16–19,40–45] Notably, despite the high OER activity of these reported catalysts, their performance enhancement typically necessitates complex synthetic approaches or the incorporation of multiple metal dopants. In contrast, the catalyst developed in this work achieved comparable OER performance through a notably simpler friction-induced amorphization method. This result highlights the effectiveness of friction-derived structural modulation, and

suggests a promising route for the *in situ* fabrication of amorphous oxide coatings and the rational design of high-performance OER catalysts.

The long-term stability of the friction-induced amorphous IrO_x layer in acidic electrolyte was further evaluated by chronopotentiometry (Fig. S10). After 15 h of continuous operation, the catalyst retained ~85% of its initial current density, which is slightly lower than that of commercial crystalline IrO_2. This behaviour likely reflects the intrinsic activity–stability trade-off of amorphous Ir-based oxides. That is, while their disordered structure and possible lattice oxygen participation during the OER can promote rapid reaction kinetics and high catalytic activity,[41,46] prolonged operation may also lead to gradual oxygen loss, partial Ir dissolution, and structural degradation. In contrast, crystalline IrO_2 generally exhibited higher durability because it predominantly follows the adsorbate evolution mechanism (AEM), which is less disruptive to the catalyst framework, although typically with lower catalytic activity.[47]

Post-OER XPS analysis was performed to evaluate the structural stability of the friction-induced IrO_x layer after OER durability testing (Fig. S11 and S12). The surface remained predominantly composed of IrO_x together with metallic Ir, consistent with the state prior to OER measurements, indicating that no significant changes in surface composition occurred during the electrochemical process. Depth-profile analysis was carried out to probe the internal structure of the IrO_x layer. Results revealed only a slight decrease in oxide-layer thickness after prolonged operation. This slight thinning may have been associated with lattice oxygen participation during the OER, which can induce partial dissolution and loss of Ir species. Nevertheless, the overall surface composition and interfacial structure were largely retained, indicating the good structural stability of the friction-induced IrO_x under acidic OER conditions.

Formation mechanism of the IrO_x layer

Based on the experimental observations shown above, the surface of rough-textured metallic Ir was prone to oxidation under the coupling effect of friction and a positive electric field. Moreover, the detailed characterization in Fig. 1 shows that oxidation products primarily occurred in the valleys between rough peaks. Hydroxide ions are key reactants on the solution side during the oxidation of Ir. Hence, modelling the electric field lines and hydroxide ion distributions on Ir surfaces with varying roughness when they serve as positive electrodes yields qualitative understanding of reactant enrichment on rougher regions.

Using classical electrochemical double-layer theory,[48,49] we showed exemplarily on line scans taken from smooth and rough samples (Fig. S13) how the changing topography of the electrode surface led to the local enrichment of hydroxide ions on rougher surface patches. Daikhin *et al.* discussed the effect of surface roughness on double-layer behaviour analytically.[50–52] We, on the other hand, solved static Poisson–Nernst–Planck systems for pure water, a binary electrolyte, for select line scans from smooth (R_a = 9 nm) and rough samples regions (R_a = 43 nm) on a sufficiently large domain with height (H) much larger than the Debye length (λ_D) directly. To mimic experimental conditions, we assumed water of pH 7 (*i.e.*, of bulk concentrations $c_{bulk} = 10^{-4}$ mol m^{-3} of H_3O^+ and OH^- alike). This means a Debye length of $\lambda_D \approx 1$ μm. To stay within the validity of the Gouy–Chapman model, we chose a small potential bias of only 0.05 V, about twice the thermal voltage at standard conditions, for our simulations presented in Fig. 4a–d. The classical continuum model would lose its validity for experimental potentials up to 1.2 V. Fig. 4a and b illustrate how equipotential lines and isoconcentration lines follow the surface roughness profile even several multiples of λ_D away from the surface on a line profile extracted along a cross-section through a rough sample.

Globally, an increased rough (true) surface area means an increased number of species, and an increased surface excess Γ compared with the flat (apparent) surface area. Locally, roughness valleys might lead to increased surface excess, while roughness peaks might lead to depletion. To illustrate this effect, we resolved surface excess locally along selected line profiles by integrating

$$\Gamma(x) = \int_{h(x)}^{H} c(x,z) - c_{bulk}\,dz \quad (1)$$

in direction z (as marked in Fig. 4a and b) on a rough electrode with profile $h(x)$ on a domain of height $H = 10\lambda_D$ in contact with an open bath. Fig. 4c and d show localized surface excess Γ for hydroxide and hydronium along a line scan on a smooth sample and on a rough sample (the latter being the same line scan treated in Fig. 4a and b). For the smoother line profile in Fig. 4c, three prominent roughness valleys exhibited obvious enrichment of hydroxide of an order of 1% compared with the mean surface excess (and depletion of hydronium at the order <1%). On the much rougher profile in Fig. 4d, local hydroxide enrichment deviated by an order of 10% from the average enrichment. Here, the locally resolved surface excess Γ fluctuated with the roughness profile on the same length scale as the roughness features, so deviations from the average were more prominent within the rougher wear track. This was expected from the concentration distribution closely following the surface topography shown in Fig. 4b.

Interchanging peaks and valleys at comparable magnitude elicited interchanging relative hydroxide depletion and enrichment. Other than for the few valleys on the smooth profile in Fig. 4c, the net effect of these fluctuations on, for example, the scale of a hypothetical wear track, was not easily discernible from the raw surface excess distribution in Fig. 4d. The delocalized trends in Fig. S14 were obtained by Gaussian process regression (GPR)[53] from the localized surface excess in Fig. 4d to illustrate net enrichment and depletion tendencies at length scales orders of magnitude beyond the Debye length. Indeed, slight relative enrichment of hydroxide in a rougher patch compared with the surrounding smoother areas was discernible.

Fig. 4e shows the evolution of local surface excess extrema in relation to the expected excess on a flat surface over a range of

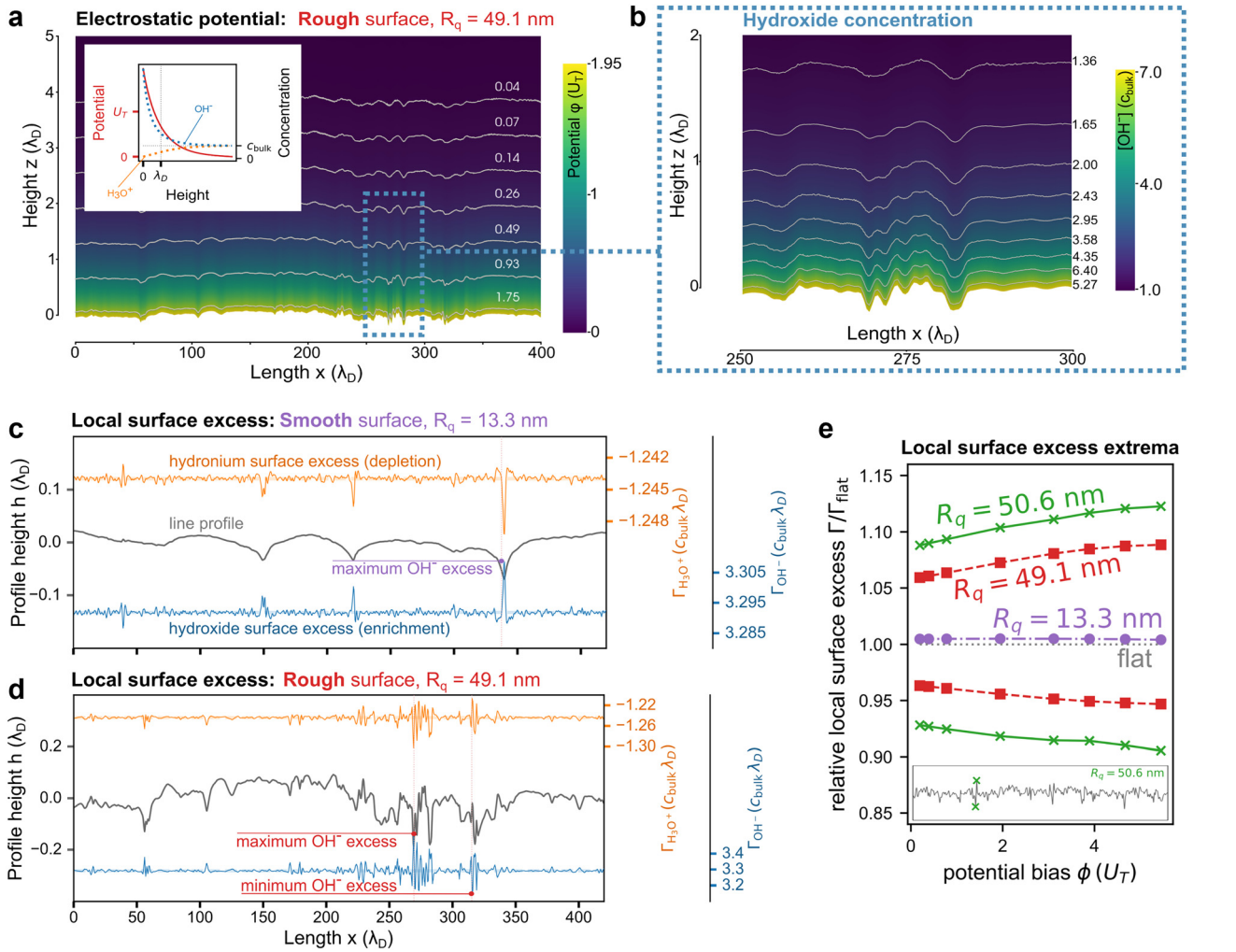

Fig. 4 Static behaviour of an electrolyte above a rough electrode. (a) Potential distribution. Color scale and white labels on top of equipotential lines show potential φ in multiples of the thermal voltage $U_T = \frac{RT}{F} \approx 25.69$ mV at temperature T = 25 °C with Faraday constant F and universal gas constant R. The inset illustrates the expected behavior for potential (red), hydronium (orange, dotted) and hydroxide (blue, dotted) concentrations on a flat electrode according to the Poisson–Boltzmann equation of classical Gouy–Chapman double layer theory. (b) Hydroxide concentration distribution within an enlarged window of (a). Color scale and black labels next to isoconcentration lines show concentration [OH^-] in units of bulk concentration c_{bulk}. In (A) and (b), the Debye length λ_D serves as the spatial unit. A potential bias of 0.05 V was applied. For water of pH 7, $\lambda_D \approx 1$ μm and $c_{bulk} = 10^{-4}$ mol m^{-3}. (c) and (d) Local surface excess. Grey lines in the middle of each plot show line profiles h taken from a (c) smooth sample (R_a = 9 nm) and (d) rough sample (R_a = 43 nm) shown in Fig. S13. Profiles are labelled with their root mean square roughness R_q. The upper (orange) and lower (blue) lines show surface excess Γ of hydronium anions (H_3O^+) and hydroxide cations (OH^-). Maximum and minimum labels on the curves indicate the position of maxima and minima of local OH^- surface excess on the respective profile. (e) Potential bias dependency of local surface excess maxima (upper curves) and minima (lower curves) of select surface profiles relative to the expected surface excess on a flat surface. Purple circular markers correspond to the local maximum on the R_q = 13.3 nm profile labelled in (c). The red square markers correspond to the local minimum and maximum on the R_q = 49.1 nm profile labelled in (d). The green crosses correspond to the local minimum and maximum on a R_q = 50.6 nm profile. The inset shows the R_q = 50.6 nm profile together with the location of its surface excess maximum and minimum on its steepest valley and peak marked by green crosses. The surface excess minimum of the comparably flat sample of R_q = 13.3 nm visually coincides with the grey dotted line for a flat surface at 1.0 and is not shown.

potentials up to 0.14 V or 5.4 U_T. The range of excess fluctuations did not behave entirely symmetrically around the flat reference. Maxima were systematically more pronounced than minima, underlining the shift of surface excess mean illustrated in Fig. S14. Scalar roughness parameters such as R_q are not sufficient to characterize the range of excess fluctuations. Instead, the range of fluctuations is governed by the steepness and curvature of single valleys and peaks. The diverging ranges of extrema for line scans of similar R_q = 49.1 nm and R_q = 50.6 nm extracted from the same rough sample emphasized this. Even for voltages one order of magnitude below the bias applied in the experiment, local excess fluctuated beyond ±10% around the flat surface reference for line scans extracted from our rough samples. The fluctuations for our R_q = 13.3 nm line scan from a smooth sample were negligible.

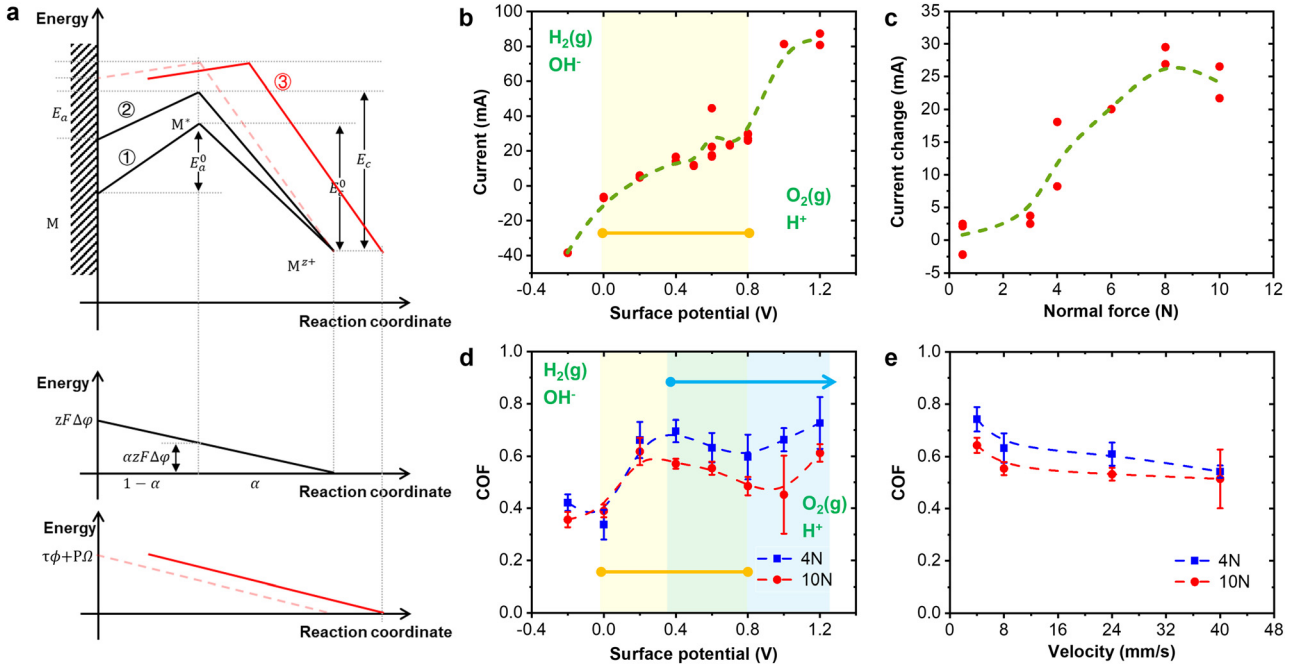

Fig. 5 Mechanism of tribo-electrochemical oxidation and the influence of experimental parameters on current and COF. (a) Reaction process under the combined influence of force and electric field. (b) Current response to variations in surface potential in the absence of external forces. (c) Effect of applied normal load on current changes during friction experiments. (d) Relationship between surface potential and COF during friction tests. (e) Influence of sliding velocity on COF in friction tests. Experiments were conducted at room temperature using a ZrO_2 ball as the upper friction pair and a roughened Ir plate as the lower friction pair. Pure water served as the lubricant and electrolyte.

In summary, our simulations qualitatively and visually demonstrate the role of surface topography in local reactant enrichment. They reveal how steep roughness valleys, with length scales comparable with the Debye length, can result in a significant increase of local hydroxide surface excess, exceeding 10% compared with a flat surface, even at small potentials around the thermal voltage. An increased density of interchanging steep valleys and peaks does not fully counterbalance enrichment and depletion of surface excess, but led to a net enrichment of surface excess over length scales much larger than the Debye length.

The reaction rate in tribo-electrochemical oxidation of metals is influenced not only by the concentration distribution of key reactants, but also by the force distribution and its effects on electrode kinetics. In previous studies,[35,36] the role of friction and electric fields in chemical reactions were explored by incorporating a tribo-electrochemical potential. Fig. 5a illustrates a model of tribo-electrochemistry based on transition state theory (or referred to as activated complex theory) and tribo-electrochemical potential in electrochemical kinetics. Curve 1 in Fig. 5a represents the chemical reaction process, Curve 2 represents the electrochemical reaction, and Curve 3 represents the tribo-electrochemical reaction. The slope of each curve indicates the likelihood of a reaction occurring.

According to the transition state theory[54], the conversion of reactant M to product M^{z+} involves passing through the transition state M^*. Without an electric field, the reaction requires energy $E_a{}^0$. However, if an electric field is applied, the energy of the reactant is raised, thereby reducing the reaction energy requirement to $\alpha F\Delta\varphi$, where α is the transfer coefficient (a parameter dependent on the chemical identity of the system), F is the Faraday constant, and $\Delta\varphi$ is the electrostatic potential difference. In conventional electrode kinetics, the effect of the electric field on the reaction potential energy is observable by comparing Curves 1 and 2.

Inspired by the thermally activated model[55], one can incorporate the work done by pressure and shear forces, represented as pressure activation energy ($P\Omega$) and shear activation energy ($\tau\phi$), respectively. This allows the tribo-electrochemical potential ($\mu_{f\&E}$) to be expressed as:

$$\mu_{f\&E} = \mu + (P\Omega + \tau\phi) + zF\varphi \quad (2)$$

where μ represents the chemical potential, P the contact pressure, τ the shear stress, Ω and ϕ are pressure and shear activation volumes, respectively, and φ is the system potential. Considering possible positional shifts of reactant and product under an applied force[56], the reaction curve transitions from the red dashed line to the solid red line shown in Curve 3 of Fig. 5a.

This analysis suggests that positive charging of the polar plate and the applied mechanical force reduce the energy barrier separating the reactants from the oxidation intermediates, thereby facilitating the reaction and increasing its probability and rate. Experiments and simulations revealed two main factors contributing to the rapid tribo-electrochemical oxidation of Ir in pure water: (1) OH^- concentrated in the

valleys of positively charged rough surface, enhancing oxidation reaction, and (2) the valleys of rough surfaces provided a more conducive environment for retaining oxidation products compared with the peaks. Further discussions will explore the relationships among surface potential, force, and current in these phenomena.

Fig. 5b illustrates the relationship between surface potential and current in the absence of external forces. As the surface potential increased from −0.2 V to +1.2 V, the current increased from −40 mA to +90 mA (for a total area of 225.0 mm^2, with the tracks area covering 0.4 mm^2). This could be interpreted as a cyclic voltammetry (CV) measurement in which the electrochemical window without an external force spanned from 0 V to 0.8 V. Fig. 5c shows the effect of applied normal load on current variation during friction experiments. By controlling the surface potential between +0.6 V and +1.2 V, we measured the change in current as the normal force increased. This increasing trend in current confirmed that a reaction occurred, and suggested that the normal load affected the Hertz contact radius, influencing current variation.

From the wear scar diameter on the upper friction ball (Fig. S15) under a 4-N load, the contact area between friction pairs was 2.7×10^{-2} mm^2. Despite this area constituting only 0.012% of the total (225.0 mm^2), it had a notable impact on results. When the normal load reached a high threshold ($\geq$8 N), the change in current became less pronounced, likely due to plastic deformation of metallic Ir. Fig. S16 shows the local plastic deformation within the wear tracks observed under a 10-N load. However, when the load was 4 N, no significant plastic deformation occurred on the smooth or rough Ir surface.

Next, we examined the influence of surface potential on the COFs in friction tests. Fig. 5d presents the variation in COFs across surface potentials ranging from −0.2 V to +1.2 V under normal loads of 4 N and 10 N, with a constant reciprocating velocity of 8 mm s^{-1}. The COF *vs.* surface potential curves fell into three regimes: (1) from −0.2 V to 0 V, the COF increased with surface potential; (2) from 0 V to +0.4 V, the COF decreased; (3) for potentials above +0.6 V, the COF rose again. According to the electrochemical potential window (Fig. 5b), reduction reactions primarily occurred between −0.2 V and 0 V, with hydrogen and OH^- generation slightly influencing COF. At this low potential, COF changes were minimal. Between 0 V and +0.4 V, COF increased due to local changes in H^+ and OH^- concentrations. At potentials over +0.6 V, tribo-electrochemical reactions produced IrO_x within wear marks, leading to a gradual COF increase under the effect of these oxides.

Fig. 5e shows the effect of sliding velocity on COF, with the surface potential held constant at +0.6 V. As the velocity increased from 4 to 40 mm s^{-1}, COF decreased, aligning with the hydrodynamic lubrication effect seen in the Stribeck curve[57]. Notably, Fig. 5d indicated that COF at 10 N was lower than at 4 N because smaller forces allowed compressive and shear stresses to accumulate on the oxide layer, resulting in a higher COF.

Based on these findings, tribo-electrochemical reactions required a suitable contact pressure. Oxidation products were challenging to generate on smooth surfaces under a 4-N load; however, on rough surfaces, this same load could create high local contact stress that accelerated Ir oxide formation. Excessively high contact pressure alone could lead to severe wear and oxide film removal. Therefore, a higher load (*e.g.*, 10 N) on a smooth surface encouraged oxide formation but also increased wear. For rough surfaces, while wear occurred at 4 N or 10 N, the products remained in valleys between peaks, making oxide presence more prominent.

Taken together, these findings highlight the potential of friction-assisted anodic processing as a more general surface engineering strategy, while also pointing to its practical boundaries. The friction-assisted anodic strategy is not limited to Ir and can be extended to other conductive metals.[35] However, it is currently more suitable for bulk or sheet substrates, while direct application to powder substrates remains challenging.

Conclusions

This study presents a novel method for the localized formation of nanostructured IrO_x layers on roughened Ir surfaces through the combined action of anodic oxidation and friction. Unlike its typical electrochemical inertness, the Ir surface undergoes rapid, localized oxidation confined to wear tracks, demonstrating the critical role of tribo-electrochemical activation. Experimental and simulation results reveal two main mechanisms facilitating this process: (1) local accumulation of OH^- in surface valleys with positive charge concentration; (2) enhanced retention of oxidation products in valleys compared with peaks.

The resulting IrO_x layers, formed within 200 s under anodic potentials, can reach sub-micrometer thickness and exhibit a unique structure: amorphous IrO_x encapsulating metallic Ir nanocrystals. Friction-induced surface defects and lowered oxidation potential further enhanced electrocatalytic activity. This structure delivers superior stability in acidic media and significantly improved the OER performance. Compared with conventional methods, this is the first approach enabling localized synthesis of nanostructured IrO_x directly on metallic Ir surfaces. Beyond advancing OER catalysis, this strategy holds promise for a range of microscale electrochemical applications, including neural electrodes, micro-reactors, and chemical sensors.

Materials and methods

Fabrication of the IrO_x layer

Tribo-electrochemical experiments were carried out on a tribometer (UMT-3, Bruker, USA) equipped with an electrochemical workstation (PGSTAT302N, Auto, Switzerland). The load applied on the ball-on-plate contact was set from 1 N to 10 N. According to the Hertzian contact model, the corresponding pressure was 499 MPa to 1075 MPa for Ir plate *vs.* ZrO_2 ball tribo-pairs. Friction tests were performed at a reciprocating frequency set from 0.2 Hz to 4 Hz over a 4-mm track. All tests

were carried out at room temperature. The surface potentials of the lower friction pairs were set from −0.8 V to +1.2 V.

Characterization

After friction tests, an optical microscope (Keyence, Japan) and a scanning electron microscope (Quanta 200, FEI, Netherlands) were used to inspect the microstructure of friction tracks. In addition, an energy-dispersive X-ray spectroscopy instrument combined with the scanning electron microscope, a high-resolution Raman spectrometer (HR Evolution, LabRAM HR Evolution, Japan), and an X-ray photoelectron spectroscopy machine (MFP-3D-SA, USA) were used to investigate elements as well as chemical compositions on the surfaces of the IrO_x layer. The sputtering rate in the XPS measurement was calibrated using thermally oxidized SiO_2 films. Surface profiles and volumes of the tribofilm were measured on a 3D optical profiling instrument (ZYGO NexView, USA). The surface chemistry states as well as the depth profiling of the tribofilms on the Ir plate were assessed *via* a ToF-SIMS machine (ION-TOF, Germany). Sputter erosion was achieved using 2-keV Cs^+ (136–139 nA). Imaging of the respective crater center was performed using a Bi^+ beam at 30 keV. The analyzer was set to detect negatively charged secondary ions. The sputtering depth was measured by the 3D optical profiling instrument after ToF-SIMS measurement.

The microstructure and compositions of a cross-section of the IrO_x layer were characterized using TEM (JEOL, Japan), after mechanical etching with FIB (QUANTA 200 FEG, FEI, Netherlands). Integrated differential phase contrast scanning transmission electron microscopy (iDPC-STEM, FEI Titan Cubed Themis G2 300, USA) was conducted in a Cs-corrected STEM operated at 300 kV. The collection angle was 51–200 mrad. The beam current was 50 pA. The dwell time was 16 μs per pixel. Elemental mapping was obtained by EDS in the same Cs-corrected STEM. The beam current was set between 10 and 15 pA to minimize damage to specimens. The dwell time was 4 μs per pixel, with a map size of 256 × 256 pixels. EDS data were integrated with Velox software.

Hydrogen and oxygen evolution reaction tests

The performance testing of the IrO_x tribofilm for the OER was conducted using LSV on a CHI-760E electrochemical workstation (CH Instruments, China). Prepared Ir–IrO_x samples were insulated with silicone rubber, with only a portion of the IrO_x tribofilm exposed to the electrolyte as the working electrode. Hg/Hg_2SO_4/saturated K_2SO_4 and Pt-net (2 × 2 cm^2) were used as the counter electrode and reference electrode, respectively. LSVs were performed in the potential window of 0.29–1.39 V at a scan rate of 5 mV s^{-1} to evaluate the OER performances, respectively, in 0.1 M $HClO_4$ (95%, Beijing Inno-Chem Technology, China).

A 1-μm diameter Pt disk electrode was used as the SECM probe (the ratio between the insulating sheath (*e.g.*, glass) and the electroactive core, defined as the RG, was 1.5) and characterized by an optical microscope (BX-51, Olympus, Japan) and steady-state voltammetry. The electrolyte was an aqueous solution of 1 mM $Ru(NH_3)_6Cl_3$ with 0.1 M K_2SO_4, using a platinum wire as the counter electrode and an Ag wire as the quasi-reference electrode. For SECM imaging, levelling of the substrate was achieved *via* constant-force feedback, with three-point levelling over an area of 6 mm × 2 mm to maintain height differences within 2 μm. The tip position was controlled by a nanoscale-precision displacement system, maintaining a consistent gap of 4 μm from the substrate *via* force-feedback. The CHI760D instrument applied a constant potential of −0.8 V *vs.* the Pt quasi-reference electrode (in $Ru(NH_3)_6Cl_3$ solution) to the probe, collecting feedback current at the tip while the substrate remained at open circuit. The scan rate was 20 μm s^{-1}, with each imaging area covering 0.5 mm × 0.2 mm.

To investigate the electrochemical reactivity of the IrO_x layer at a higher resolution, SECM (Guangdong Dynechem Electronic Technology China) was introduced. A quartz-insulated Pt-disk probe (diameter = 25 μm, RG ≈ 9) and the prepared Ir–IrO_x plate were connected as the two working electrodes, while a Hg/Hg_2SO_4/saturated K_2SO_4 and a Pt-wire were the reference electrode and counter electrode, respectively. The feedback mode of SECM was applied to position the Pt-disk probe at 15 μm above the sample in a 0.1 M KCl (99.8%, Beijing Inno-Chem Technology, China) containing 5 mM $K_3[Fe(CN)_6]$ (99.5%, Tianjin Rgent Chemicals, China) solution. The SG-TC mode of SECM was applied to accurately inquire the onset potentials of the OER over IrO_x with the background Ir plate for comparison. A quartz-insulated Pt-disk probe (diameter = 25 μm, RG ≈9) and the prepared Ir–IrO_x plate were connected as the two working electrodes, while a Hg/Hg_2SO_4/saturated K_2SO_4 and a Pt-wire were the reference electrode and counter electrode, respectively. The Pt-disk probe was at 15 μm above the sample. The Pt-disk probe was constantly held at 0.13 V (E_{probe}) during the OER study, aiming at measuring the O_2 evoked at the sample by water splitting. Simultaneously, LSV at the sample was recorded in the potential range of 0.59–1.09 V ($E_{substrate}$) at a scan rate of 5 mV s^{-1} in 0.1 M $HClO_4$. To map the local reactivity distribution of the IrO_x–Ir sample, an area of 500 × 500 μm^2 (*X*–*Y* direction) with an increment of 25 μm was scanned. The sample potential was kept at 0.78 V, 0.79 V and 0.80 V for the OER, while the potential polarized at the Pt-disk probe was the same as described previously. The potentials reported in the experiments were referenced to the Hg/Hg_2SO_4/saturated K_2SO_4 electrode (Tianjin Aida Hengsheng Technology Development, China), while the potentials described in the results were converted to the reversible hydrogen electrode (RHE) using the formula: $E = E_0 + E_{Hg/Hg_2SO_4} + 0.059 \times pH$, where E_0 is the potential measured relative to Hg/Hg_2SO_4/saturated K_2SO_4, and E_{Hg/Hg_2SO_4} is the standard potential of Hg/Hg_2SO_4/saturated K_2SO_4 (0.652 V).

SECM mapping and controlled macroscopic measurements using a masking strategy consistently confirmed that the enhanced electrocatalytic activity originated predominantly from the friction-induced IrO_x regions rather than the unmodified Ir substrate.

Simulation

Smooth and rough samples have been published.[58,59] Scalar metrics of line profiles were extracted with contact.engineering[60].

Discretization meshes were generated with gmsh[61]. Static Poisson–Nernst–Planck systems were solved by the classical finite elements method with the electrochemistry module of matscipy[62] and DOLFINx.[63–66] Gaussian process regression was carried out with gpflow[67]. Data analyses were facilitated by checkpointing with ADIOS4DOLFINx[68] and workflow management with Snakemake[69]. The simulation workflow has been published[70].

Author contributions

C. L., Y. T. and Y. M provided the conception and designed the experiments. C. L. performed the experiments, analysed the data, and wrote a draft of the manuscript. J. L. H. performed the simulations, and wrote the simulation part of the manuscript. H. P., H. X, L. H. and X. C. carried out the hydrogen and oxygen evolution reaction tests. H. P. and X. C. wrote the electrocatalytic part of the manuscript. J. C. provided guidance on mechanisms. H. Z., Y. T. and Y. M. improved the whole manuscript. C. L., Y. M. and Y. T. supervised the experiments. All authors discussed the results and implications, and commented on the manuscript at all stages.

Conflicts of interest

The authors declare no competing interests.

Data availability

All data needed to evaluate the conclusions are present in the paper and its supplementary information (SI). Supplementary Fig. S1–S16 and Table S1 provide detailed data on the preparation, characterization, mechanical properties, electrochemical activity, and stability of the friction-assisted electrochemically formed IrO_x layer, including comparisons with Ir and IrO_2. Supplementary references are included. See DOI: https://doi.org/10.1039/d6mh00036c.

Additional related data may be requested from the authors.

Acknowledgements

This work has been financially supported by National Natural Science Foundation of China (52105193), China Postdoctoral Science Foundation (2021TQ0175) and Canada Research Chairs Program. Chenxu Liu thanks Dongping Zhan for discussion of the hydrogen and oxygen evolution reaction tests. Johannes L. Hörmann thanks Hadi Yassine, Andreas Greiner, and Lars Pastewka for discussions and validation of simulation results. Hongbo Zeng acknowledges support from the Canada Research Chairs Program.

References

1 C. Liang, R. R. Rao and K. L. Svane, *et al.*, Unravelling the effects of active site density and energetics on the water oxidation activity of iridium oxides, *Nat. Catal.*, 2024, **7**, 763, DOI: 10.1038/s41929-024-01168-7.

2 R. V. Mom, L. J. Falling and O. Kasian, *et al.*, Operando structure–activity–stability relationship of iridium oxides during the oxygen evolution reaction, *ACS Catal.*, 2022, **12**, 5174, DOI: 10.1021/acscatal.1c05951.

3 Y.-R. Zheng, J. Vernieres and Z. Wang, *et al.*, Monitoring oxygen production on mass-selected iridium–tantalum oxide electrocatalysts, *Nat. Energy*, 2021, **7**, 55, DOI: 10.1038/s41560-021-00948-w.

4 S. Lee, Y. J. Lee and G. Lee, *et al.*, Activated chemical bonds in nanoporous and amorphous iridium oxides favor low overpotential for oxygen evolution reaction, *Nat. Commun.*, 2022, **13**, 3171, DOI: 10.1038/s41467-022-30838-y.

5 H. N. Nong, T. Reier and H.-S. Oh, *et al.*, A unique oxygen ligand environment facilitates water oxidation in hole-doped IrNiOx core–shell electrocatalysts, *Nat. Catal.*, 2018, **1**, 841, DOI: 10.1038/s41929-018-0153-y.

6 K. H. Saeed, M. Förster and J. F. Li, *et al.*, Water oxidation intermediates on iridium oxide electrodes probed by in situ electrochemical SHINERS, *Chem. Commun.*, 2020, **56**, 1129, DOI: 10.1039/c9cc08284k.

7 A. Li, S. Kong and K. Adachi, *et al.*, Atomically dispersed hexavalent iridium oxide from MnO_2 reduction for oxygen evolution catalysis, *Science*, 2024, **384**, 666, DOI: 10.1126/science.adg5193.

8 C. Hu, K. Yue and J. Han, *et al.*, Misoriented high-entropy iridium ruthenium oxide for acidic water splitting, *Sci. Adv.*, 2023, **9**, eadf9144, DOI: 10.1126/sciadv.adf9144.

9 H. Tao, B. Hu and N. Zheng, Strain creates excellent catalysts for electrolyzers, *Joule*, 2021, **5**, 3072, DOI: 10.1016/j.joule.2021.11.010.

10 M. Faustini, M. Giraud and D. Jones, *et al.*, Hierarchically structured ultraporous iridium-based materials: A novel catalyst architecture for proton exchange membrane water electrolyzers, *Adv. Energy Mater.*, 2018, **9**, 1802136, DOI: 10.1002/aenm.201802136.

11 E. Willinger, C. Massue and R. Schlogl, *et al.*, Identifying key structural features of IrO_x water splitting catalysts, *J. Am. Chem. Soc.*, 2017, **139**, 12093, DOI: 10.1021/jacs.7b07079.

12 H. N. Nong, L. J. Falling and A. Bergmann, *et al.*, Key role of chemistry versus bias in electrocatalytic oxygen evolution, *Nature*, 2020, **587**, 408, DOI: 10.1038/s41586-020-2908-2.

13 J. Gao, C. Q. Xu and S. F. Hung, *et al.*, Breaking long-range order in iridium oxide by alkali ion for efficient water oxidation, *J. Am. Chem. Soc.*, 2019, **141**, 3014, DOI: 10.1021/jacs.8b11456.

14 C. Ma, W. Sun and W. Qamar Zaman, *et al.*, Lanthanides regulated the amorphization-crystallization of IrO2 for outstanding OER performance, *ACS Appl. Mater. Interfaces*, 2020, **12**, 34980, DOI: 10.1021/acsami.0c08969.

15 V. Pfeifer, T. E. Jones and S. Wrabetz, *et al.*, Reactive oxygen species in iridium-based OER catalysts, *Chem. Sci.*, 2016, **7**, 6791, DOI: 10.1039/c6sc01860b.

16 H. Zhang, P. Song and X. Mei, *et al.*, Amorphous–crystalline interface coupling of $IrNiO_x/WO_3$ for efficient and stable

acidic water splitting, *ACS Catal.*, 2025, **15**, 12395, DOI: 10.1021/acscatal.5c02782.
17 G. Yu, R. Li and Y. Hu, *et al.*, Supporting IrO_x nanosheets on hollow TiO_2 for highly efficient acidic water splitting, *Nano Res.*, 2024, **17**, 6903, DOI: 10.1007/s12274-024-6681-7.
18 Z. Zhuang, Y. Wang and C. Q. Xu, *et al.*, Three-dimensional open nano-netcage electrocatalysts for efficient pH-universal overall water splitting, *Nat. Commun.*, 2019, **10**, 4875, DOI: 10.1038/s41467-019-12885-0.
19 G. Liu, L. Chen and Z. Liu, *et al.*, Short-range-engineered Nd-doped IrO_x enables oxide path mechanism for high-performance PEM water electrolysis, *Small*, 2026, **22**, e11956, DOI: 10.1002/smll.202511956.
20 Y. S. Li, N. R. Tao and K. Lu, Microstructural evolution and nanostructure formation in copper during dynamic plastic deformation at cryogenic temperatures, *Acta Mater.*, 2008, **56**, 230, DOI: 10.1016/j.actamat.2007.09.020.
21 H. W. Zhang, Z. K. Hei and G. Liu, *et al.*, Formation of nanostructured surface layer on AISI 304 stainless steel by means of surface mechanical attrition treatment, *Acta Mater.*, 2003, **51**, 1871, DOI: 10.1016/s1359-6454(02)00594-3.
22 X. Chen, Z. Han and X. Li, *et al.*, Lowering coefficient of friction in Cu alloys with stable gradient nanostructures, *Sci. Adv.*, 2016, **2**, e1601942, DOI: 10.1126/sciadv.1601942.
23 T. H. Fang, W. L. Li and N. R. Tao, *et al.*, Revealing extraordinary intrinsic tensile plasticity in gradient nano-grained copper, *Science*, 2011, **331**, 1587, DOI: 10.1126/science.1200177.
24 J. E. Baur and T. W. Spaine, Electrochemical deposition of iridium (IV) oxide from alkaline solutions of iridium(III) oxide, *J. Electroanal. Chem.*, 1998, **443**, 208.
25 L. M. Zhang, Y. S. Gong and C. B. Wang, *et al.*, Substrate temperature dependent morphology and resistivity of pulsed laser deposited iridium oxide thin films, *Thin Solid Films*, 2006, **496**, 371, DOI: 10.1016/j.tsf.2005.09.076.
26 L. C. Seitz, C. F. Dickens and K. Nishio, *et al.*, A highly active and stable $IrO_x/SrIrO_3$ catalyst for the oxygen evolution reaction, *Science*, 2016, **353**, 1011, DOI: 10.1126/science.aaf5050.
27 S. Thanawala, D. G. Georgiev and R. J. Baird, *et al.*, Characterization of iridium oxide thin films deposited by pulsed-direct-current reactive sputtering, *Thin Solid Films*, 2007, **515**, 7059, DOI: 10.1016/j.tsf.2007.02.090.
28 R. K. Kawar, P. S. Chigare and P. S. Patil, Substrate temperature dependent structural, optical and electrical properties of spray deposited iridium oxide thin films, *Appl. Surf. Sci.*, 2003, **206**, 90.
29 M. Dai, J. Xia and Z. Xue, *et al.*, Improved iridium/iridium oxide pH electrode through supercritical treatment, *J. Electroanal. Chem.*, 2022, **922**, 116740, DOI: 10.1016/j.jelechem.2022.116740.
30 S. Hao, H. Sheng and M. Liu, *et al.*, Torsion strained iridium oxide for efficient acidic water oxidation in proton exchange membrane electrolyzers, *Nat. Nanotechnol.*, 2021, **16**, 1371, DOI: 10.1038/s41565-021-00986-1.
31 J. Xu, H. Jin and T. Lu, *et al.*, IrO_x·nH2O with lattice water–assisted oxygen exchange for high-performance proton exchange membrane water electrolyzers, *Sci. Adv.*, 2023, **9**, eadh1718.
32 A. R. Harris, A. G. Paolini and G. G. Wallace, Effective area and charge density of iridium oxide neural electrodes, *Electrochim. Acta*, 2017, **230**, 285, DOI: 10.1016/j.electacta.2017.02.002.
33 I. S. Lee, J. C. Park and G. H. Lee, *et al.*, Neural cells on iridium oxide, *Key Eng. Mater.*, 2003, **254–256**, 805, DOI: 10.4028/www.scientific.net/KEM.254-256.805.
34 J. M. Zhang, C. J. Lin and Z. D. Feng, *et al.*, Mechanistic studies of electrodeposition for bioceramic coatings of calcium phosphates by an in situ pH-microsensor technique, *J. Electroanal. Chem.*, 1998, **452**, 235.
35 C. Liu, Z. Zhu and W. Ouyang, *et al.*, Friction-induced electrochemical activation of platinum group metals via electromechanical coupling, *Mater. Today*, 2026, DOI: 10.1016/j.mattod.2026.103323.
36 C. Liu, Y. Tian and Y. Meng, A Chemical potential equation for modeling triboelectrochemical reactions on solid-liquid interfaces, *Front. Chem.*, 2021, **9**, 650880, DOI: 10.3389/fchem.2021.650880.
37 Z. Pavlovic, C. Ranjan and Q. Gao, *et al.*, Probing the structure of a water-oxidizing anodic iridium oxide catalyst using Raman spectroscopy, *ACS Catal.*, 2016, **6**, 8098, DOI: 10.1021/acscatal.6b02343.
38 P. C. Liao, C. S. Chen and W. S. Ho, *et al.*, Characterization of IrO_2 thin films by Raman spectroscopy, *Thin Solid Films*, 1997, **301**, 7.
39 J. Augustynski, M. Koudelka and J. Sanchez, *et al.*, ESCA study of the state of iridium and oxygen in electrochemically and thermally formed iridium oxide films, *J. Electroanal. Chem. Interfacial Electrochem.*, 1984, **160**, 233.
40 W. Sun, Z. Wang and X. Tian, *et al.*, In situ formation of grain boundaries on a supported hybrid to boost water oxidation activity of iridium oxide, *Nanoscale*, 2021, **13**, 13845, DOI: 10.1039/d1nr01795k.
41 M. Sun, H. Huang and X. Niu, *et al.*, Grain boundary-derived local amorphization enhances acidic OER, *ACS Catal.*, 2024, **14**, 15764, DOI: 10.1021/acscatal.4c03746.
42 M.-G. Kim, H. J. Lee and T. K. Lee, *et al.*, Iridium selenium oxyhydroxide shell for polymer electrolyte membrane water electrolyzer with low Ir loading, *ACS Energy Lett.*, 2024, **9**, 2876, DOI: 10.1021/acsenergylett.4c00884.
43 G. Wu, X. Zheng and P. Cui, *et al.*, A general synthesis approach for amorphous noble metal nanosheets, *Nat. Commun.*, 2019, **10**, 4855, DOI: 10.1038/s41467-019-12859-2.
44 X. Han, T. Mou and A. Islam, *et al.*, Theoretical prediction and experimental verification of IrO_x supported on titanium nitride for acidic oxygen evolution reaction, *J. Am. Chem. Soc.*, 2024, **146**, 16499, DOI: 10.1021/jacs.4c02936.
45 F. Xue, X. Guo and B. Min, *et al.*, Unconventional high-index facet of iridium boosts oxygen evolution reaction: How the facet matters, *ACS Catal.*, 2021, **11**, 8239, DOI: 10.1021/acscatal.1c01867.
46 Y. Kim, J. Kim and S. I. Choi, *et al.*, Structure dependent accessibility of active sites governs catalytic activity and

stability of iridium oxides in the acidic oxygen evolution reaction, *J. Am. Chem. Soc.*, 2026, **148**, 957, DOI: 10.1021/jacs.5c16721.

47 K. Zhang, X. Liang and Y. Wang, *et al.*, Support-tuned iridium reconstruction with crystalline phase dominating acidic oxygen evolution, *Nat. Commun.*, 2025, **16**, 8164, DOI: 10.1038/s41467-025-63541-9.

48 M. Gouy, Sur la constitution de la charge électrique à la surface d'un électrolyte, *J. Phys. Theor. Appl.*, 1910, **9**, 457, DOI: 10.1051/jphystap:019100090045700.

49 D. L. Chapman, A contribution to the theory of electrocapillarity, *Lond. Edinb. Dubl. Phil. Mag.*, 1913, **25**, 475, DOI: 10.1080/14786440408634187.

50 L. I. Daikhin, A. A. Kornyshev and M. Urbakh, Nonlinear Poisson–Boltzmann theory of a double layer at a rough metal/electrolyte interface: A new look at the capacitance data on solid electrodes, *J. Chem. Phys.*, 1998, **108**, 1715, DOI: 10.1063/1.475543.

51 L. I. Daikhin, A. A. Kornyshev and M. Urbakh, Double layer capacitance on a rough metal surface: Surface roughness measured by ''Debye ruler'', *Electrochim. Acta*, 1997, **42**, 2853, DOI: 10.1016/S0013-4686(97)00106-0.

52 L. I. Daikhin, A. A. Kornyshev and M. Urbakh, Double-layer capacitance on a rough metal surface, *Phys. Rev. E:Stat. Phys., Plasmas, Fluids, Relat. Interdiscip. Top.*, 1996, **53**, 6192, DOI: 10.1103/PhysRevE.53.6192.

53 J. Hensman, N. Fusi and N. D. Lawrence, Gaussian processes for big data, in *Proceedings of the Twenty-Ninth Conference on Uncertainty in Artificial Intelligence (UAI-13)*, AUAI Press, 2013, DOI: 10.48550/arXiv.1309.6835.

54 A. J. Bard, L. R. Faulkner and H. S. White, *Electrochemical methods: Fundamentals and applications*, Wiley, 2022.

55 B. J. Briscoe and D. C. B. Evans, The shear properties of Langmuir-Blodgett layers, *Proc. R. Soc. Lond. A*, 1982, **380**, 389, DOI: 10.1098/rspa.1982.0048.

56 C. Bustamante, Y. R. Chemla and N. R. Forde, *et al.*, Mechanical processes in biochemistry, *Annu. Rev. Biochem.*, 2004, **73**, 705, DOI: 10.1146/annurev.biochem.72.121801.161542.

57 X. Lu, M. M. Khonsari and E. R. M. Gelinck, The Stribeck curve: Experimental results and theoretical prediction, *J. Tribol.*, 2006, **128**, 789, DOI: 10.1115/1.2345406.

58 C. Liu, J. L. Hörmann and H. Pan, *et al.*, Iridium smooth sample Ra = 9 nm (version 1), *contact.engineering*, 2024, DOI: 10.57703/CE-BUZ3K.

59 C. Liu, J. L. Hörmann and H. Pan, *et al.*, Iridium rough sample Ra = 43 nm (version 1), *contact.engineering*, 2024, DOI: 10.57703/CE-48TYE.

60 M. C. Röttger, A. Sanner and L. A. Thimons, *et al.*, Contact.engineering—Create, analyze and publish digital surface twins from topography measurements across many scales, *Surf. Topogr.:Metrol. Prop.*, 2022, **10**, 035032, DOI: 10.1088/2051-672X/ac860a.

61 C. Geuzaine and J. F. Remacle, Gmsh: A 3-D finite element mesh generator with built-in pre- and post-processing facilities, *Int. J. Numer. Meth. Eng.*, 2009, **79**, 1309, DOI: 10.1002/nme.2579.

62 P. Grigorev, L. Frérot and F. Birks, *et al.*, Matscipy: materials science at the atomic scale with Python, *J. Open Source Software*, 2024, **9**, 5668, DOI: 10.21105/joss.05668.

63 I. A. Baratta, J. P. Dean and J. S. Dokken, *et al.*, DOLFINx: The next generation FEniCS problem solving environment, *Zenodo*, 2023, DOI: 10.5281/zenodo.10447665.

64 M. W. Scroggs, J. S. Dokken and C. N. Richardson, *et al.*, Construction of Arbitrary order finite element degree-of-freedom maps on polygonal and polyhedral cell meshes, *ACM Trans. Math. Software*, 2022, **48**, 1, DOI: 10.1145/3524456.

65 M. W. Scroggs, I. A. Baratta and C. N. Richardson, *et al.*, Basix: a runtime finite element basis evaluation library, *J. Open Source Software*, 2022, **7**, 3982, DOI: 10.21105/joss.03982.

66 M. S. Alnæs, A. Logg and K. B. Ølgaard, *et al.*, Unified form language: A domain-specific language for weak formulations of partial differential equations, *ACM Trans. Math. Software*, 2014, **40**(2), 1–37, DOI: 10.1145/2566630.

67 A. G. D. G. Matthews, M. V. D. Wilk and T. Nickson, *et al.*, GPflow: A Gaussian process library using tensorflow, *J. Mach. Learn. Res.*, 2017, **18**(40), 1–6.

68 J. S. Dokken, ADIOS4DOLFINx: A framework for checkpointing in FEniCS, *J. Open Source Software*, 2024, **9**, 6451, DOI: 10.21105/joss.06451.

69 F. Molder, K. P. Jablonski and B. Letcher, *et al.*, Sustainable data analysis with Snakemake, *F1000Res*, 2021, **10**, 33, DOI: 10.12688/f1000research.29032.2.

70 J. L. Hörmann, jotelha/pnp-on-rough-surfaces (version 0.1.0), *Zenodo*, 2024, DOI: 10.5281/zenodo.14108618.

